Available online at www.sciencedirect.com

ScienceDirect

Journal of Magnesium and Alloys 10 (2022) 3406–3417

www.elsevier.com/locate/jma

Full Length Article

Corrosion and tribocorrosion resistance of MAO-based composite coating on AZ31 magnesium alloy

Siqin Liu[a,c], Guihua Li[b,c], Yuming Qi[a,c], Zhenjun Peng[a], Yinping Ye[b], Jun Liang[a,c,*]

[a] State Key Laboratory of Solid Lubrication, Lanzhou Institute of Chemical Physics, Chinese Academy of Sciences, Lanzhou 730000, PR China
[b] Key Laboratory of Science and Technology on Wear and Protection of Materials, Lanzhou Institute of Chemical Physics, Chinese Academy of Sciences, Lanzhou 730000, PR China
[c] Center of Materials Science and Optoelectronics Engineering, University of Chinese Academy of Sciences, Beijing 100049, PR China

Received 18 November 2020; received in revised form 24 February 2021; accepted 9 April 2021
Available online 10 June 2021

Abstract

In this paper, a multi-functional composite coating with low friction coefficient, high wear resistance and excellent tribocorrosion resistance is fabricated on AZ31 Mg alloys by micro-arc oxidation and spray-coating methods. The microstructure, and composition of the coating are characterized by SEM, EDS, XRD, and FT-IR. Potentiodynamic polarization and EIS tests are conducted to evaluate the corrosion resistance of the composite coating. The tribocorrosion property is also studied using pin-on-disk tribometer in 3.5 wt.% NaCl solution. It is found that the composite coating possesses better long-term corrosion resistance than the single MAO coating. The tribocorrosion tests prove that the composite coating exhibits much better wear and tribocorrosion resistance than the single MAO coating and can protect the substrate from corrosion under a sliding condition.

Keywords: Magnesium alloy; Micro-arc oxidation; Composite coating; Corrosion; Tribocorrosion.

1. Introduction

Magnesium (Mg) alloys have been paid much attention to weight restricted applications, such as aerospace and automotive components, due to their low-density, high strength-to-weight ratio, good machinability, and high thermal conductivity [1]. Unfortunately, inherent poor corrosion and wear resistance of Mg alloys limit their life cycle and increases the maintenance cost, which has blocked the wide range of applications [2–5]. Nowadays, many surface treatment technologies, including anodizing, micro-arc oxidation, vapor deposition, conversion films, and electroplating, have been proposed to improve corrosion and wear resistance of Mg alloys [6–11]. Meanwhile, Mg alloys with different coatings can be damaged or completely destroyed due to the surface rubbing or sliding in corrosive environment, allowing galvanic couple to be established between Mg alloys and surrounding passive areas, which remarkably accelerates the corrosion rate of Mg alloys [12]. Hence, intensive research into tribocorrosion mechanisms is needed to protect the Mg alloys used as engineering components from harsh environments.

The micro-arc oxidation (MAO) process, also known as plasma electrolytic oxidation (PEO), could generate thick and adherent ceramic-like coatings on the surface of light-weight metals (Al, Mg, and Ti) under high voltages in environmentally friendly electrolytes, such as silicate, phosphate, and aluminate [13]. In general, the ceramic-like coating comprises an inner barrier layer and an outer porous layer [14]. The MAO coating can separate the substrate from the corrosive environment to provide corrosion protection. However, the micropores in the coating act as the pathway of the corrosion agents

* Corresponding author at: State Key Laboratory of Solid Lubrication, Lanzhou Institute of Chemical Physics, Chinese Academy of Sciences, Lanzhou 730000, PR China.
E-mail address: jliang@licp.cas.cn (J. Liang).

https://doi.org/10.1016/j.jma.2021.04.004

and lead to the deterioration of corrosion protection [15]. In addition, the most impressive advantage of MAO coating is that the oxide film is formed under the condition of high temperature and high pressure on the surface of the substrate, resulting in a greater adhesion of the film than other surface treatment technologies such as vapor deposition, spraying and so on [16]. To date, a variety of composite coatings have been developed based on MAO coatings, including sol-gel coatings, polymer coatings, electro- and electroless deposited coatings, electrophoretic coatings, etc. [16–20]. Ning et al. [21] deposited pure diamond-like carbon (DLC), H-DLC, Si-DLC, and Cr-DLC films on the MAO coated-Mg alloys using closed field unbalance magnetron sputtering system, respectively. Results showed that these DLC films did not completely seal the surface micropores of MAO coatings but could reduce their number and pore size. The duplex MAO/DLC films further improved corrosion and wear protection to Mg alloys. Jiang et al. [22] developed a self-healing composite coating on Mg alloy through incorporation of the corrosion inhibitor 8-HQ into the MAO and silica coating. Kim et al. [23] fabricated a composite coating by combining MAO process and hydrothermal treatment to improve corrosion resistance and bioactivity of Mg alloy. In summary, introducing a top film to the MAO coating on Mg alloy not only could provide good anti-corrosion performance but also it could give other properties, including superhydrophobic, wear resistance, bioactivity, and self-healing functions etc. However, up to now, few attentions have been paid to the tribocorrosion behavior of composite coatings based on MAO coating on Mg alloys. Therefore, in order to make Mg alloys more competitive in application, it is valuable to develop a composite coating based on the MAO coating which possess excellent protection abilities to the Mg alloys in harsh environments.

In this paper, a multi-functional polymeric sealing film for the MAO coating on AZ31 Mg alloys is fabricated by spray-coating. The polymer coating is comprised of polyamide-imide (PAI) and polytetrafluoroethylene (PTFE), resulting in that the composite coating owns hydrophobicity, low friction coefficient, and high wear resistance besides excellent corrosion resistance. The tribocorrosion behavior is studied using pin-on-disk friction experiments in 3.5 wt.% NaCl solution.

2. Material and methods

2.1. Materials

Magnesium alloy AZ31 B (composition: 3.12% Al, 0.94 % Zn, 0.29 % Mn, 0.0029 % Fe, 0.013 % Si, 0.0029 % Cu, 0.00046 % Ni, and the rest is Mg) specimens with a size of 20 × 20 × 2 mm were used as substrates. The specimens were sequentially ground from #120 to #1000 with SiC sandpaper and ultrasonically cleaned in ethanol and distilled water. Sodium Phosphate and KF were supplied by Tianjin Fengyue Chemicals Co., Ltd (Shanghai, China). Polyamide-imide (PAI) and polytetrafluoroethylene (PTFE) provided by Sino-rich Technology Co., Ltd (Beijing, China) and Shandong Huafu Fluoro-Chemical Co., Ltd (Shandong, China), respectively. N, N-dimethylformamide, and N-methyl pyrrolidone were acquired from Tianjin Kemiou Chemical reagent Co., Ltd (Tianjin, China).

2.2. MAO process

The MAO process was performed to prepare oxide coating using a pulsed bi-polar power source, a beaker with 1 L capacity, and a stainless-steel condenser as the electrolyte cell and cooling system, respectively. The electrolyte was prepared using 0.04 M Na_3PO_4 in distilled water with addition of 1 g/L KOH and 1g/L KF. The cooling system was used to keep the temperature of the electrolyte solution at 20 ± 2 °C. Oxide coatings were produced at a constant positive current density of 8 A/dm^2 and negative density of 4 A/dm^2 with other electrical parameters: frequency 200 Hz and duty cycle 30 %. In order to ensure that the final coatings with and without polymer coating have the same total thickness, the MAO coatings with the thicknesses of around 15 and 35 μm were prepared by using processing time 9 and 12 min, respectively.

2.3. Post-treatment process

For the preparation of polymer coatings, polyamide-imide (PAI) and polytetrafluoroethylene (PTFE) were uniformly dispersed in 20 mL of the mixed solvents (the mixture of N, N-dimethylformamide and N-methyl pyrrolidone with volume ratio of 1:1) to obtain a slurry. The final solid content of the mixing slurry was adjusted to about 20 wt.%. Next, the mixed slurry was sprayed onto the surface of MAO coated AZ31 alloy, driven by pure N_2 with stable pressure about 0.15 MPa. The sprayed wet specimens were then cured in a drying oven at 130 °C for 10 h. The thickness of the sprayed polymer coating was 15 ± 5 μm, making the total thickness of composite coating was as the same as that of the single MAO coating without polymer coating (35 ± 5 μm). The single MAO coating without polymer coating and composite coating with polymer coating were denoted as MAO and MAO-PP, respectively.

2.4. Characterization

The surface and cross-section morphologies of the composite coating were observed by a scanning electron microscope (SEM, JSM-5600LV) employed at 20 keV. The element composition and distribution of the composite coating were determined by energy dispersive spectrometer (EDS , Kevex), which was attached in SEM. The phase composition of the coatings was analyzed by X-Ray Diffractometer (XRD, Rigaku D/Max-2400) at a grazing angle of 3° with Cu Kα radiation (40 kV, 40 mA) within the range of 10°–90°. The chemical bond information of the composite coating was assured by the Fourier transform infrared spectroscopy (FT-IR, Nicolet IS5 Thermo Scientific) with an attachment of attenuated total reflection in the wavenumber range from 4000 to 400 cm^{-1}. The water contact angles (WCAs) of the sample surfaces were measured by an optical contact angle measuring

device (DSA100) with a water droplet of 4 μL in volume. The adhesion strengths for the polymer coating on MAO coated and uncoated Mg alloy were measured by an adhesive shear testing device (Elcometer 508), and the tests for each specimen were conducted in triplicate to ensure the reproducibility of results.

Potentiodynamic polarization and electrochemical impedance spectroscopy (EIS) tests were conducted using an Autolab PGSTAT302N electrochemical workstation to evaluate the corrosion behavior of the specimens with a three-electrode cell composed by an Ag/AgCl (saturated with KCl) reference electrode, a platinum counter electrode and the specimen as the working electrode. The specimens were immersed in 3.5 wt.% NaCl solution with exposed area. of 1 cm^2 by using a home-made electrolytic cell. The electrolytic cell had a circular hole with an area of 1 cm^2, making the exposed area of the specimens to the corrosive solution equal to the area of the circular hole. Each specimen was immersed in the NaCl solution for 30 min at 298 K, allowing the system to be stabilized. The potentiodynamic polarization tests were performed from -2.0 to -0.3 V (vs. Ag/AgCl) at a scanning rate of 1 mV/s. EIS tests were operated at open circuit potential with the signal amplitude of 10 mV over a frequency ranging from 100,000 to 0.01 Hz on specimens after different immersion durations to understand the degradation phenomena. The experimental impedance plots were fitted to equivalent circuits using the Zview software. All the electrochemical tests were repeated at least three times to ensure good reproducibility.

The tribocorrosion behaviors of the specimens were investigated by the integrated UMT-TriboLab tribometer and Autolab PGSTAT302N electrochemical workstation at room temperature. The counterpart Si_3N_4 ball (Φ 4 mm) was fixed by a holder and vertically contacted with the specimen surface that was immersed in 3.5 wt.% NaCl solution. The exposed area during the corrosive wear test was around 1.2 cm^2 controlled by the electrolytic cell matched with the tribometer. The specific parameters of the tribometer were set as follows: reciprocating amplitude of 2.0 mm, average speed of 3 mm/s, and loads of 5 N, 10 N, and 15 N. The corrosion behaviors of samples during friction were evaluated by the potentiodynamic polarization tests, which were recorded from -2.0 to -0.3 V (vs. Ag/AgCl) at a scanning rate of 1 mV/s, using the same three-electrode cell with the above electrochemical test.

3. Results and discussion

3.1. Surface and cross-sectional microscopy

Fig. 1 (a) and (c) show the surface SEM morphologies and contact angle of MAO and MAO-PP samples, respectively. A highly porous surface is produced by MAO process, as shown in Fig. 1 (a), which is attributed to the formation of discharge channels during MAO process [24]. Corrosive agents could easily penetrate the MAO coating through the micropores, leading to corrosion of the substrate. Also, it can be seen that

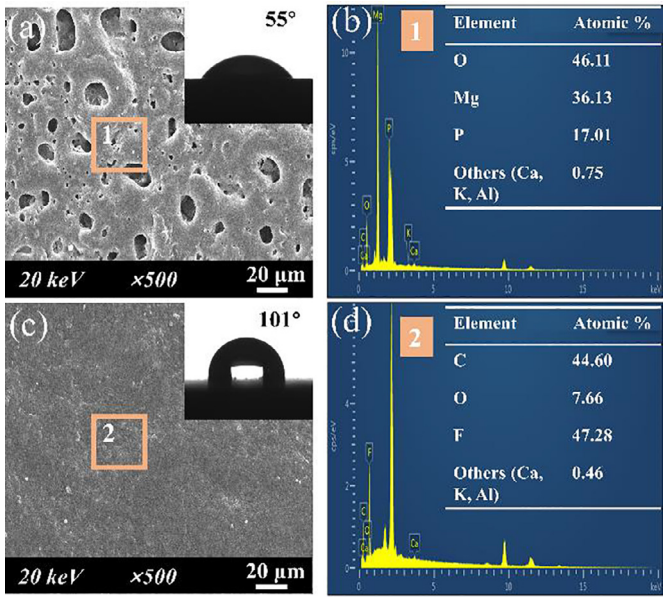

Fig. 1. SEM images and contact angle (insert) of MAO (a) and MAO-PP (c), and EDS spectrum and element content of region 1 (b) and region 2 (d).

the MAO coating produced in phosphate solution is mainly composed of Mg, P, and O elements according to the EDS results, as presented in Fig. 1 (b). As shown in Fig. 1 (c), the compact polymer coating completely covers the MAO coating and no apparent micro-cracks are found on the surface of the coating, which could effectively prevent the corrosive agents from permeating into the substrate. The polymer coating is mainly composed of C, O, and F elements according to the EDS results, as presented in Fig. 1 (d). Moreover, water contact angles were measured by an optical contact angle meter to investigate the influence of the polymer coating on the surface wettability. Surface wettability would affect the penetration of corrosive medium into the coating and thus play an important role on the corrosion anti-performance [25,26]. As shown in the insert images in Fig. 1 (a) and (c), the MAO coating is a hydrophilic surface with a contact angle of 55°, while the polymer coating exhibits a hydrophobic surface with a contact angle of 101° due to the low surface energy of C-F alkyl chain in PTFE [27].

Fig. 2 shows the cross-sectional SEM images with EDS elemental mappings of MAO coating and the composite coating. As shown in Fig. 2(a), the MAO coating is uneven in thickness with around 35 ± 3 μm. Besides, it can be seen that the elements of Mg, O, and P uniformly disperse in the MAO coating according to the results of EDS elemental mappings. For the composite coating as presented in Fig. 2(b), the interface between MAO coating with thickness of 15 ± 3 μm and polymer coating with thickness of 20 ± 3 μm could be easily distinguished. Meanwhile, the polymer coating firmly adheres to the MAO coating (with the adhesion strength of 2.1 ± 0.6 MPa) and no visible crack except a few pores appear in the interface between MAO coating and polymer coating.

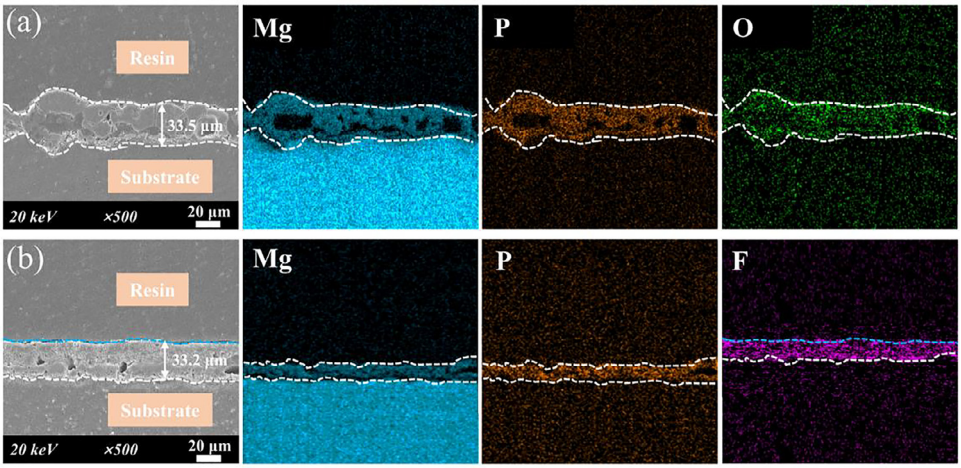

Fig. 2. Cross-sectional SEM images with EDS elemental mappings of MAO sample (a) and MAO-PP sample (b).

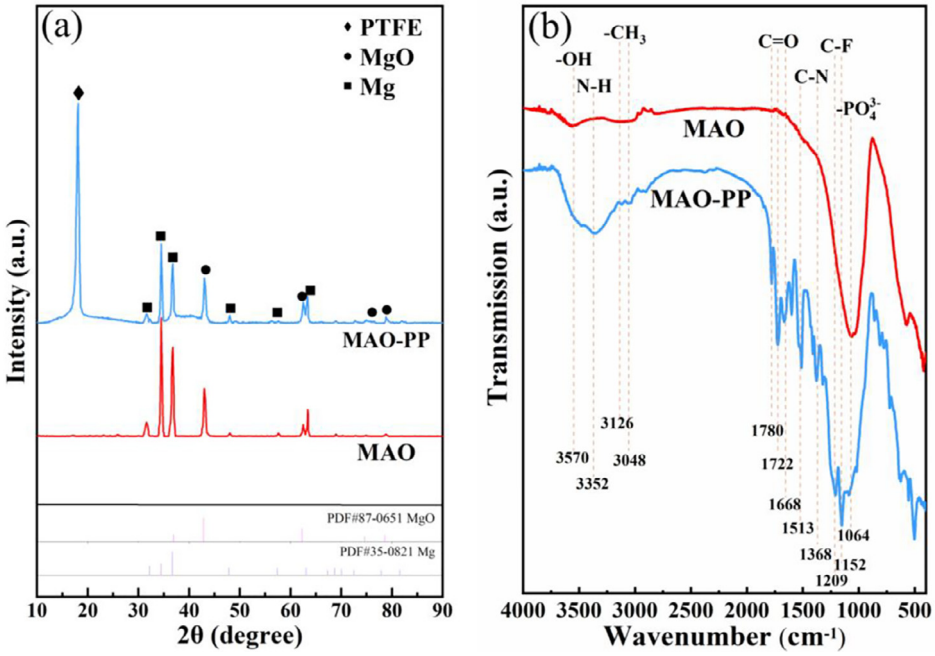

Fig. 3. XRD patterns (a) and FT-IR spectra (b) of MAO sample and MAO-PP sample.

3.2. Structure and composition of coating

Fig. 3 (a) and (b) show the XRD patterns and FT-IR spectra of MAO and MAO-PP samples, respectively. The MAO coating produced from phosphate electrolyte mainly consists of crystalline MgO and amorphous phosphate compounds according to the XRD and FT-IR results, indicating that the growth of MAO coating in phosphate electrolyte mainly depends on the oxidation of the Mg alloy substrate and deposition of PO_4^{3-}. The strong diffraction peaks corresponding to the Mg substrate are also recorded in Fig. 3 (a) for the MAO and MAO-PP samples, revealing that X-ray could reach the substrate through the oxide coating. The intensive peaks at $2\theta=18°$ presented in XRD patterns, and the bands at 1209 cm^{-1} and 1152 cm^{-1} of C-F bond in FTIR spectra for the MAO-PP sample are related to the PTFE [28,29]. Moreover, the N-H band at 3532 cm^{-1}, the C-N bands at 1668 cm^{-1} and 1513 cm^{-1}, the asym C=O band at 1780 cm^{-1} and sym C=O band at 1722 cm^{-1} of imide, and the sym C=O band at 1668 cm^{-1} of amide presented in Fig. 3 (b) are attributed to the existence of PAI in the coating of MAO-PP sample [30].

3.3. Electrochemical corrosion behavior

The corrosion resistance of the MAO and MAO-PP samples is evaluated by potentiodynamic polarization tests in 3.5 wt.% NaCl solution. Fig. 4 shows the potentiodynamic polarization curves of AZ31 Mg alloy, MAO, and MAO-PP samples immersed in 3.5 wt.% NaCl solution. And electro-

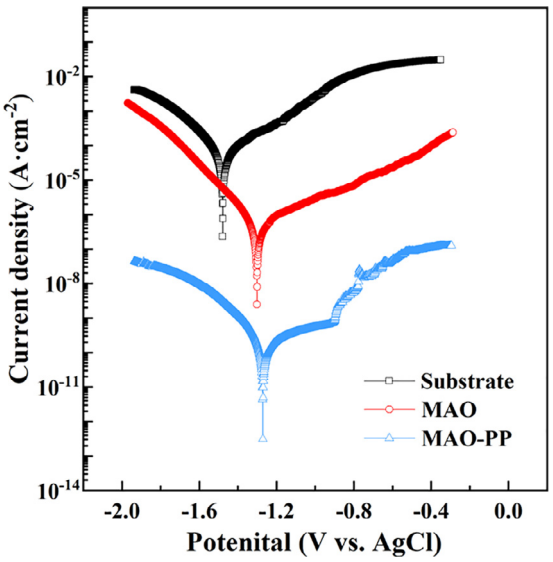

Fig. 4. Potentiodynamic polarization curves of AZ31 Mg alloy, MAO and MAO-PP samples immersed in 3.5 wt.% NaCl solution.

chemical corrosion parameters, including E_{corr} and i_{corr} values are fitted by Tafel extrapolation and listed in Table 1. AZ31 Mg alloy substrate possesses the highest i_{corr} (9.450 × 10^{-5} A cm^{-2}) and the most negative E_{corr} (-1.482 V) values. The i_{corr} significantly decreases to 8.17 × 10^{-7} A cm^{-2} and the E_{corr} positively shifts to -1.301 V after MAO process. Compared to the MAO sample, the MAO-PP sample exhibits the lowest i_{corr} value (6.68 × 10^{-10} A cm^{-2}), which is five orders of magnitude lower than the substrate and the most positive E_{corr} (-1.219 V). Such a significant enhancement of corrosion resistance would be attributed to the synergistic protection of MAO coating and dense polymer coating, which can more effectively prevent the corrosive medium from permeating into the substrate than the single MAO coating [31].

Table 1.
Fitting results of potentiodynamic curves in 3.5 wt.% NaCl solution.

Samples	E_{corr} (V vs. AgCl)	i_{corr} (A cm^{-2})
AZ31 alloy substrate	-1.482 ± 0.01	(9.45 ± 0.8) × 10^{-5}
MAO	-1.301 ± 0.02	(8.17 ± 1.8) × 10^{-7}
MAO-PP	-1.219 ± 0.02	(6.68 ± 1.1) × 10^{-10}

The long-term corrosion stability of the composite coating is evaluated by electrochemical impedance spectroscopy (EIS) tests in 3.5 wt.% NaCl solution. Fig. 5 shows the typical Bode plots for the two samples after 1, 96, 192, and 288 h immersion in 3.5 wt.% NaCl solution. In general, impedance modulus in the high frequency region reflects the property of

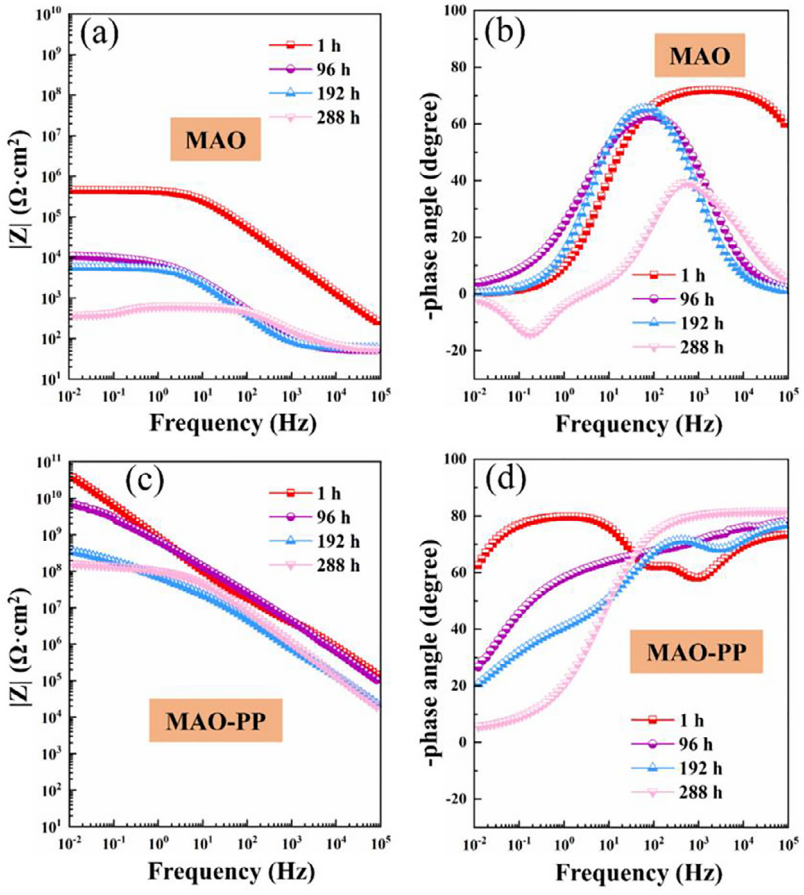

Fig. 5. Bode plots of MAO sample (a) and (b), and MAO-PP sample (c) and (d) at different immersion time in 3.5 wt.% NaCl solution.

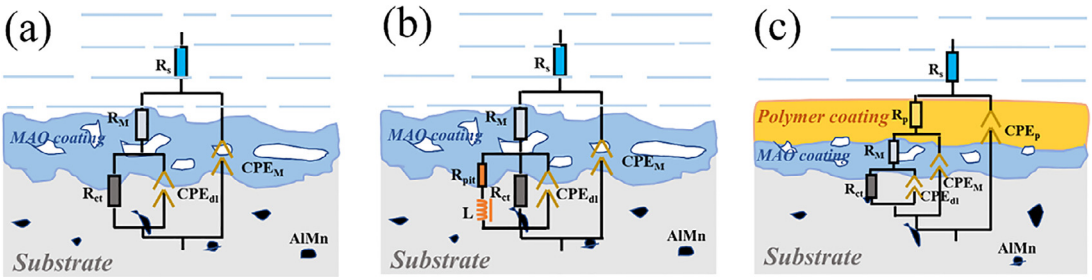

Fig. 6. Equivalent circuits used to fit EIS plots and physical models for MAO sample (a) and (b), and MAO-PP sample (c) during immersion tests.

the coating of its compactness, and the impedance modulus at the low frequency zone is related to the ability of corrosion resistance [32]. As shown in Fig. 5 (a) and (c), both samples show the same trend of decreasing impedance modulus at low frequency ($|Z|_{f\to 0}$) with the increasing of immersion time. The $|Z|_{f\to 0}$ of MAO sample reduced from 10^5 to 10^2 Ω•cm^2, while the $|Z|_{f\to 0}$ of MAO sample reduce from 10^{10} to 10^8 Ω•cm^2 after 288 h immersion in 3.5 wt.% NaCl solution, indicating that the MAO-PP sample possess much better long-term corrosion resistance than the MAO sample [22].

The corrosion processes of the two samples could be investigated by the equivalent circuits, according to the characteristics of their Bode plots, as shown in Fig. 6, where R_s, R_p, R_M and R_{ct} represent solution resistance, polymer coating resistance, MAO coating resistance, and charge-transfer resistance, respectively. For the MAO sample, the equivalent circuit is characterized by two constant-phase elements (CPE) in the early immersion stage (1 h, and 96 h),as shown in Fig. 6 (a). CPE_{coat} and CPE_{dl} represent the capacitive elements at the interface of MAO coating/solution and Mg alloy/solution, respectively [33]. After a longer immersion time (192 h and 288 h), new circuit composed of L and R_{pit} is introduced to represent the localized dissolution of Mg alloy as shown in Fig. 6(b), where L is related to the adsorption-desorption process of Cl^- ions on substrate and R_{pit} represents pitting corrosion resistance [34]. For the MAO-PP sample, a new constant-phase element (CPE_p) is introduced in the equivalent circuit to represent the capacitive elements at the interface of polymer coating and solution, as shown in Fig. 6(c) and the equivalent circuit has no change with the increase of immersion time.

By fitting the EIS plots, R_{ct} values of the two samples at different immersion time are obtained, as shown in Fig. 7, which are the pivotal parameters to evaluate the corrosion resistance of samples. It can be seen that the R_{ct} values of the MAO sample and MAO-PP sample are approximately 10^{11} and 10^4 Ω•cm^2 at the initial immersion tests, respectively. The R_{ct} values of the two samples decrease gradually with the increasing of immersion time. However, the MAO-PP sample has almost 5 orders of magnitude higher R_{ct} values than the MAO sample at the same immersion time. This means that the composite coating shows more excellent corrosion protection performance than the single MAO coating.

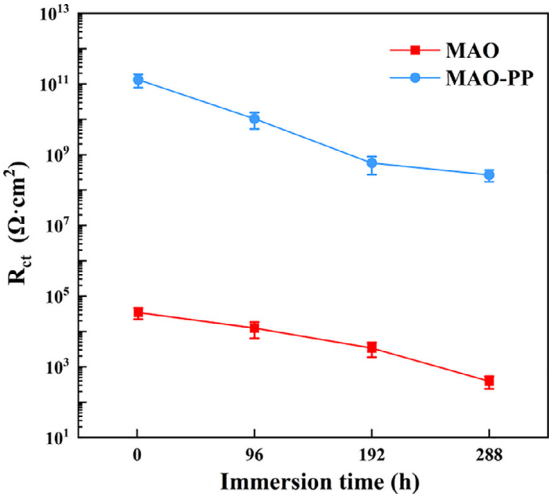

Fig. 7. The evolution of R_{ct} values of the MAO and MAO-PP samples as a function of immersion time in 3.5 wt.% NaCl solution.

3.4. Tribocorrosion behavior

Open circuit potential (OCP) and potentiodynamic polarization tests were used to investigate the corrosion behavior during the sliding process of the MAO and MAO-PP samples. OCP could provide the information related to the state of surface electrochemistry, and polarization curve could reflect the changes in the corrosion resistance of the samples under sliding conditions [35].

Fig. 8 shows the evolution of OCP before, during, and after sliding with coefficient of friction under different loads in 3.5 wt.% NaCl solution for different samples. As shown in Fig. 8 (a), the average coefficient of friction (COF) of the MAO sample under 5 N load is 0.4 and there are no obvious fluctuations during sliding, indicating that the MAO coating is not worn out under 5 N load after 2400 s of sliding. The EDS elemental mappings and element content of wear track also confirm this result, as shown in Fig. 9 (a). Nevertheless, the COF exhibited sharp fluctuations from 0.2 to 1.0 at the load of 10 N, which could attribute to the displacement of the counterpart ball through the coating-substrate interface [36] and thus indicate that the MAO coating has been worn out. Meanwhile, the OCP maintains at -1.35 V under 5 N

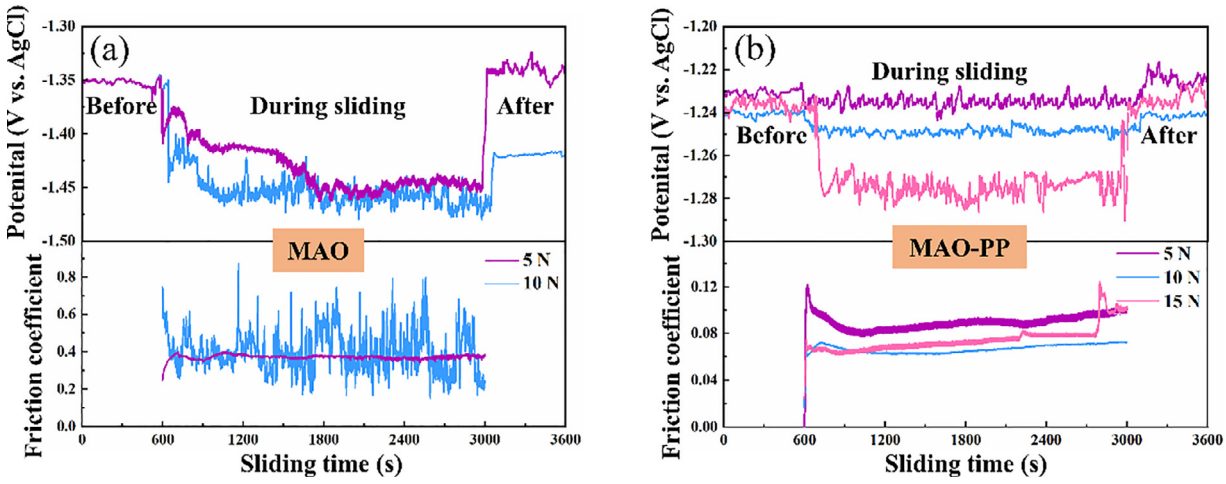

Fig. 8. Variation of OCP with time recorded before, during, and after sliding under different loads in 3.5 wt.% NaCl solution with the COF values of MAO (a) and MAO-PP (b).

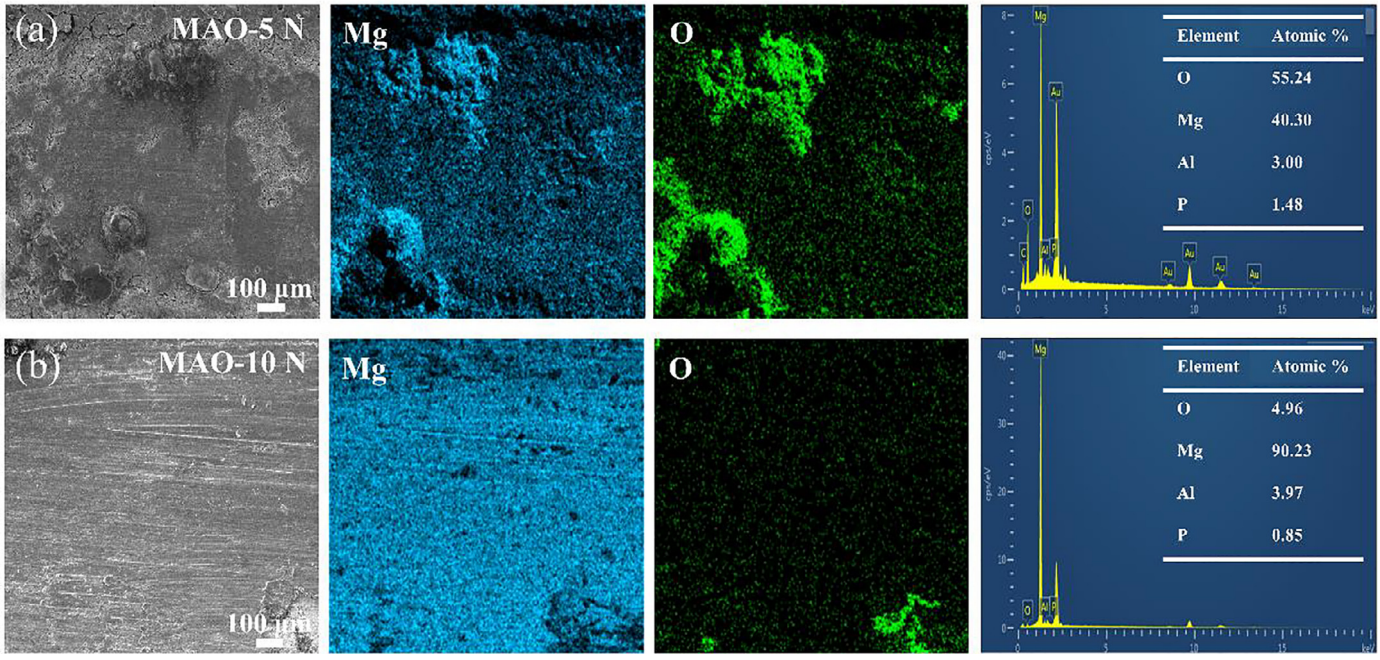

Fig. 9. SEM morphology, EDS elemental mapping and spectroscopy of worn surfaces for MAO sample under 5 N load (a) and under 10 N load (b) after tribocorrosion.

and 10 N loads before sliding. As sliding began, however, the OCP of the MAO sample under 5 N load decreases gradually from -1.35 V to -1.45 V in 1200 s sliding process and is stable at this level from 1200 s to 2400 s. The step-like decrease of OCP may be attributed to the continuous establishment of new equilibriums between the depassivation and repassivation as the coating thickness decreased during sliding. The OCP of the MAO sample under 10 N load also stabilizes at about -1.45 V in the sliding process from 900 s to 2400 s. When the sliding process finished, the OCP of MAO under 5 N load increases to the value of -1.34 V which is close to the value before sliding, revealing that the state of MAO coating surface electrochemistry has not been changed significantly before and after sliding. But when the load increased to 10 N, the OCP of the MAO sample decreases 0.075 V compared to the value of -1.35 V before sliding and maintains at -1.425 V, which means that the electrochemistry state of MAO coating surface has been destroyed. The SEM morphology and EDS spectrum/mappings of wear track of the MAO sample presented in Fig. 9 (b) also reveal that the MAO coating has been worn out under 10 N load.

The average COF of the MAO-PP sample under 5 N and 10 N loads are 0.08 and 0.06, respectively, as shown in Fig. 8 (b). The lower COF is attributed to the lubricating effect of PTFE [37]. Besides, the OCPs under 5 N and 10 N loads are stable at about -1.235 V and -1.250 V during

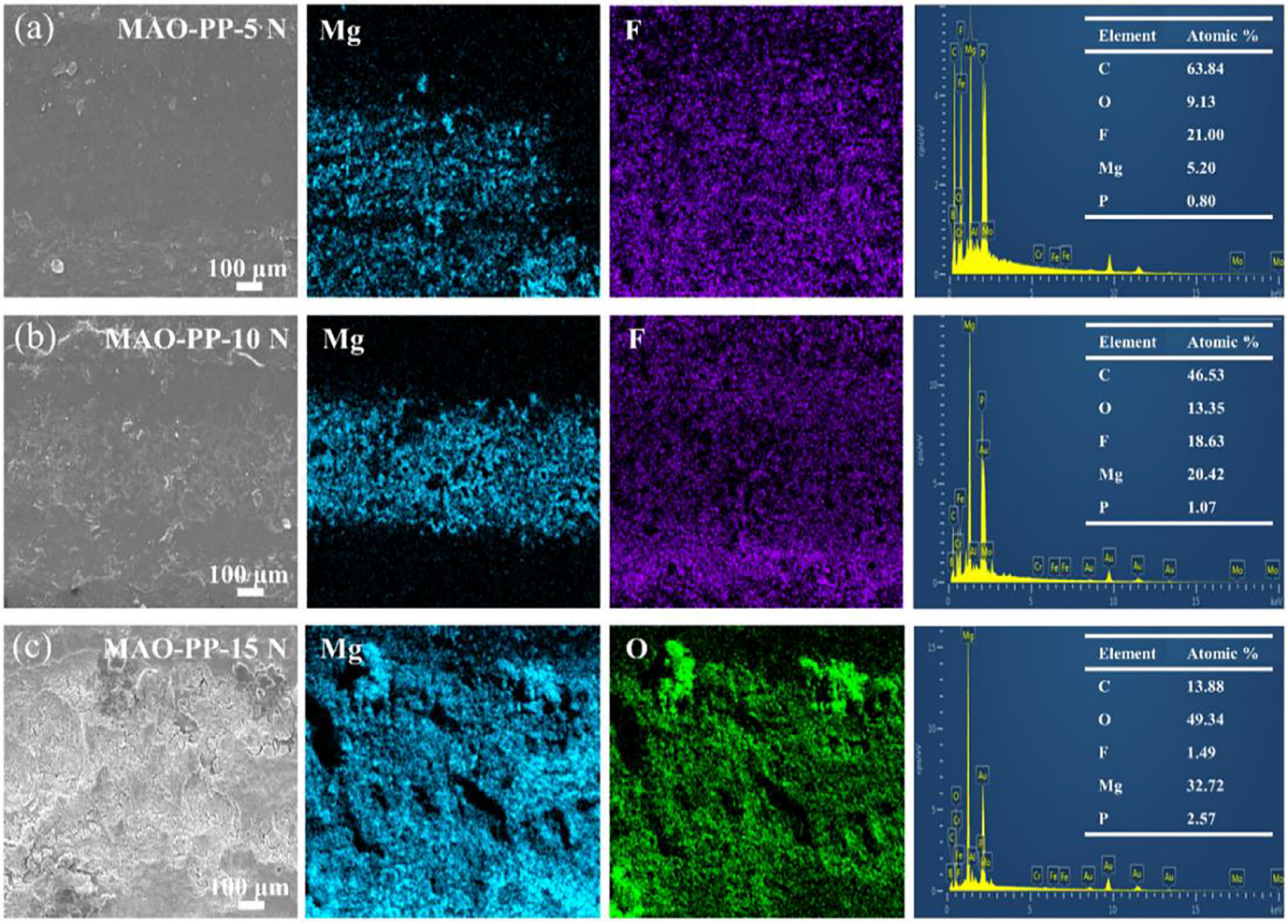

Fig. 10. SEM morphology, EDS elemental mapping, and spectroscopy of worn surfaces for MAO-PP sample under 5 N load (a), under 10 N load (b), and under 15 N load (c) after tribocorrosion.

sliding, respectively, which are very close to the OCPs before sliding, respectively. The OCPs under 5 N and 10 N loads after sliding restore to the values of -1.225 V and -1.245 V, respectively. The evolutions of COF and OCP of the MAO-PP sample under 5 N and 10 N loads reveal that there are almost no changes on the electrochemical and physical states of surface due to the excellent lubrication behavior of polymer coating [38]. When the load increases to 15 N, the OCP value decreases from -1.238 V to -1.280 V, and the drop in OCP is higher than the changes under 5 N and 10 N loads. Besides, the COF suddenly increases from 0.08 to 0.12 after 2750 s sliding and then fluctuates with the sliding time. The sudden increase of the COF could be attributed to the wearing out of the polymer coating, which is confirmed by the EDS spectra analysis of wear track as shown in Fig. 10 (c). With the increase of loads, the content of C and F elements decrease, while the content of Mg, O and P elements increase, as shown in Fig. 10 (a–c). This reveals that the thickness of the polymer coating continuously reduces and finally the MAO coating is exposed at higher loading.

Fig. 11 and Fig. 12 show the 3D surface profiles of the wear tracks and cross-sections for the MAO sample and MAO-PP sample under different loads, respectively. It can be seen that the width and depth of wear tracks for MAO-PP sample are both much smaller than that for the MAO sample due to its lower friction coefficient and higher tribocorrosion resistance. Fig. 13 presents the cross-sectional morphology of the wear tracks for the MAO sample and MAO-PP sample under 10 N load. As shown in Fig. 13 (a), the depth of wear track of the MAO sample is more than 40 μm, which is larger than the MAO coating thickness, indicating that the MAO coating is worn out and the Mg alloy substrate suffers from severe corrosive wear under 10 N load. By contrast, the depth of wear track of the MAO-PP sample is around 20 μm according to Fig. 13 (b), which means that the MAO coating as the interlayer is hardly destroyed during tribocorrosion under 10 N load.

The potentiodynamic polarization curves and corresponding fitting results of the MAO and MAO-PP samples at different sliding loads are presented in Fig. 14. It can be seen from Fig. 14 (a) and (c) that the i_{corr} values of the MAO sam-

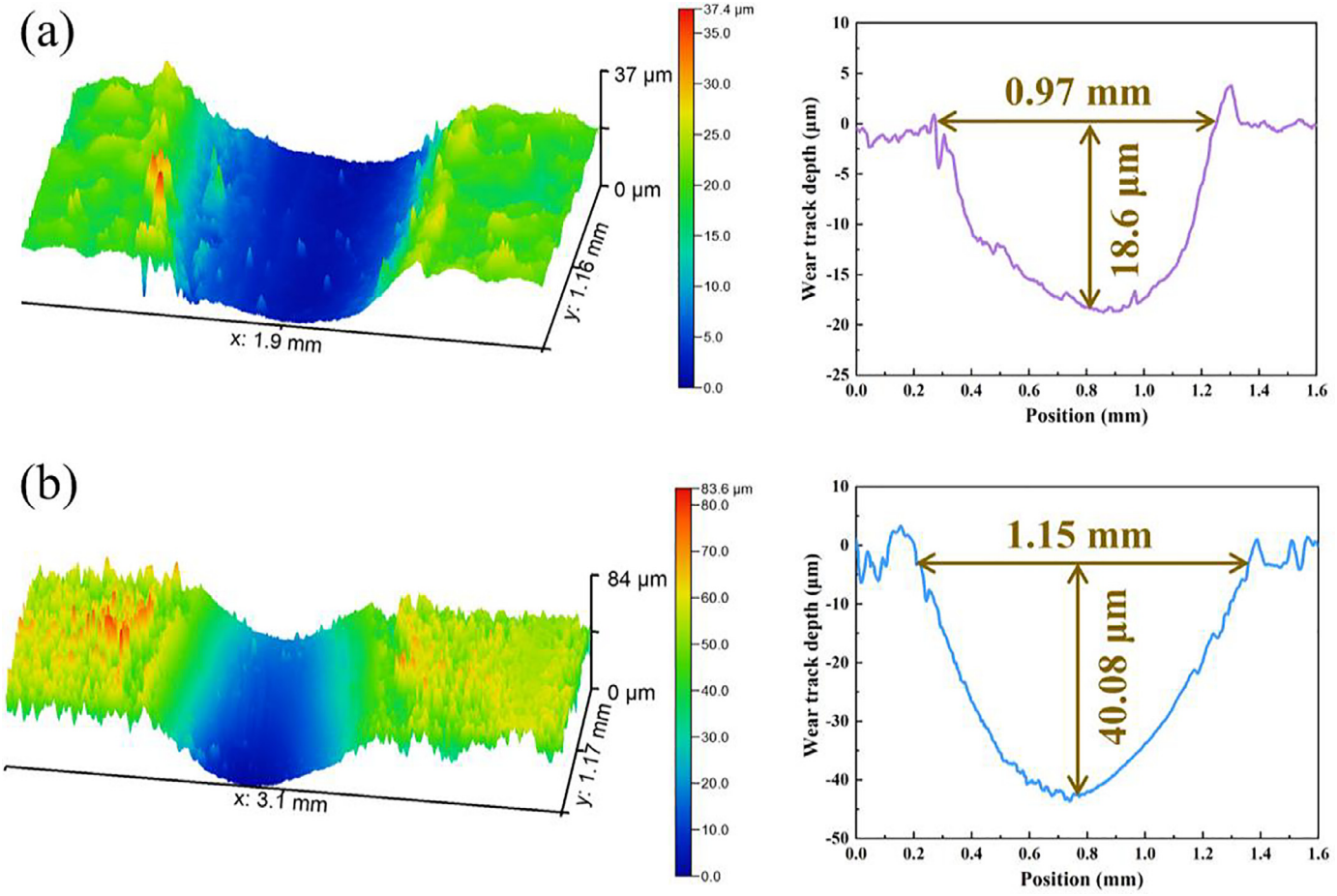

Fig. 11. 3D morphologies of the wear tracks and cross-sections for the MAO sample under 5 N load (a) and under 10 N load (b) after tribocorrosion.

ple under 5 N and 10 N loads increases by approximately 3 and 4 orders of magnitude compared to that without load, respectively. Especially, the i_{corr} value under 10 N load is even lower than that of the Mg alloy substrate, suggesting that the MAO coating could no longer protect the substrate from corrosion. For the MAO-PP sample, Fig. 14 (b) and (c) shows that the E_{corr} under 5 N, 10 N, and 15 N loads during tribocorrosion are all more positive than that of the Mg alloy substrate. However, the E_{corr} shifts to more negative sides with the increase of the sliding loads. Generally, the E_{corr} corresponds to the thermodynamic tendency to corrosion of coated samples [39,40]. Negative shift of the E_{corr} indicates the deterioration of corrosion resistance of the coating. Interestingly, the MAO-PP sample under 5 N load has more or less the same E_{corr} as that without load, which suggests that the relatively lower load during sliding did not deteriorate the corrosion resistance of the composite coating. Besides, the MAO-PP sample has lower i_{corr} values under 5 N and 10 N loads but similar i_{corr} value with the Mg alloy substrate. This reveals that the composite coating has better corrosion protection performance than the single MAO coating and has not been worn out under the load of 5 N and 10 N loads during tribocorrosion. On the other hand, the composite coating could not provide protection to the substrate from tribocorrosion under a load of 15 N.

3.5. Corrosion and tribocorrosion protection mechanism

Based on the above results, it could conclude that the composite coating significantly enhances the corrosion resistance, wear resistance, and tribocorrosion resistance of the Mg alloys. The corrosion and tribocorrosion protection mechanisms of the MAO coating and composite coating are proposed based on the microstructure, electrochemical, and tribo-electrochemical analysis of the coating and the schematics are presented in Fig. 15. When the MAO sample immersed in the 3.5 wt.% NaCl solution, the corrosive medium like Cl^- ions would permeate into the micro-pores and destroy the micro-structure of the MAO coating with the increasing of immersion time, as shown in Fig. 15 (a). And then, the Cl^- ions could reach the interface between the MAO coating and Mg alloy substrate, leading to a localized corrosion of Mg alloy according to the reaction 1 [2]. The formation of corrosive product $Mg(OH)_2$ would continue to destroy the MAO coating because of its larger molar volume than the MgO [41]. The composite coating, however, could effectively prevent the Cl^- ions from penetrating into the interface between the MAO coating and Mg alloy substrate due to the synergistic protection of MAO coating and dense polymer coating, as illustrated in Fig. 15 (b).

$$Mg + 2H_2O \rightarrow Mg(OH)_2 + H_2 \uparrow \quad (1)$$

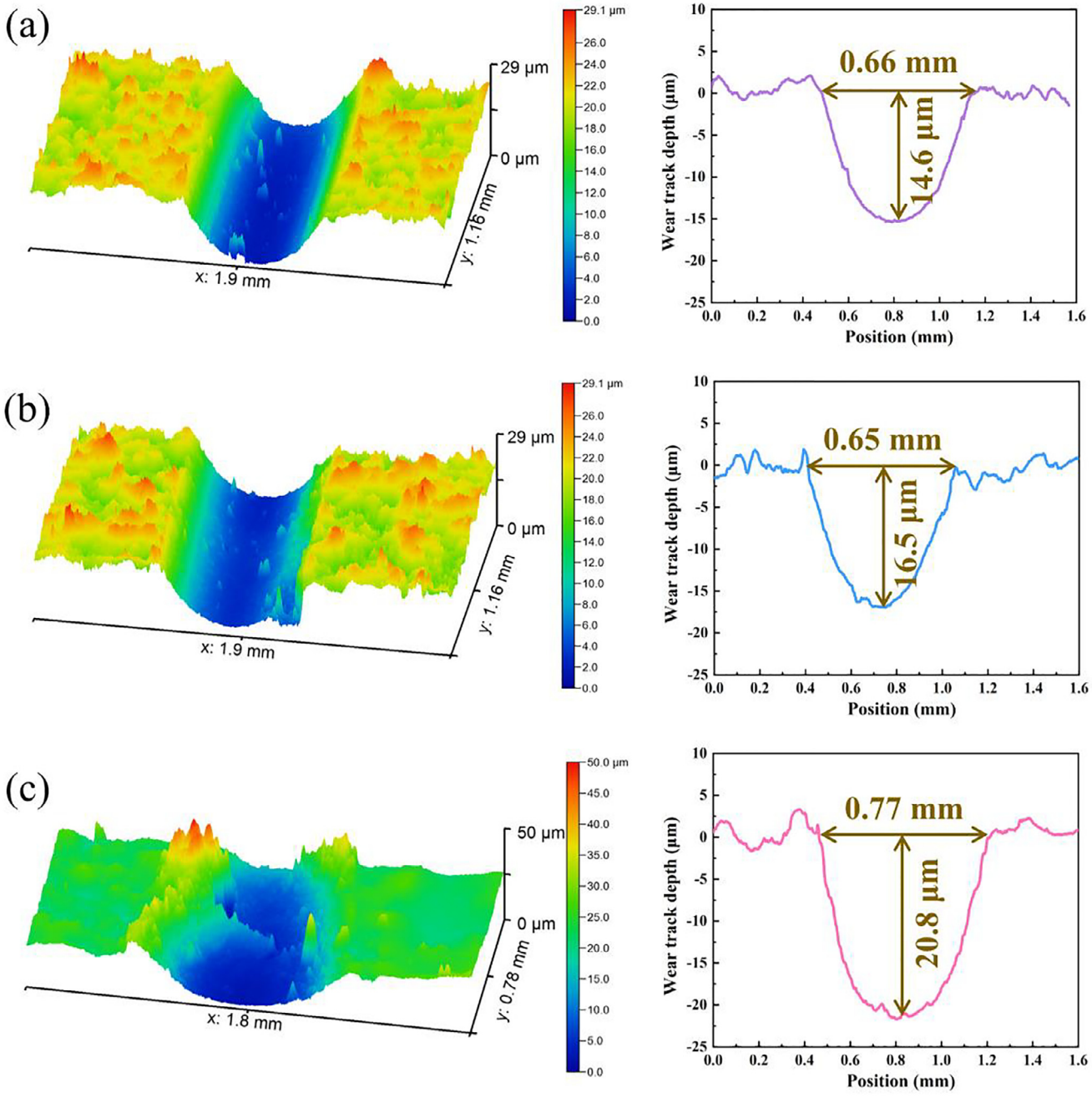

Fig. 12. 3D morphologies of the wear tracks and cross-sections for the MAO-PP sample under 5 N load (a), under 10 N load (b) and under 15 N load (c) after tribocorrosion.

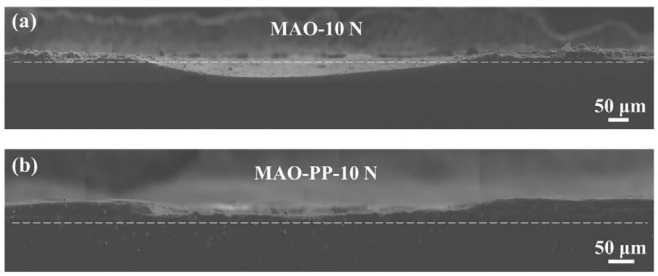

Fig. 13. Cross-sectional surface morphology of the wear tracks for MAO sample (a) and MAO-PP sample (b) under 10 N load.

The tribocorrosion process with a load of 10 N is taken as an example to analyze the protection of the two coating on the substrate. As shown in Fig. 16 (a), MAO coating is worn out according to the evolution of COF and OCP during sliding, as well as the EDS analysis. During tribocorrosion, OCP is a mixed potential that reveals the relatively stable state between active worn areas and passive unworn areas [42]. And a galvanic coupling is established between the mechanically depassivated areas (anode) and the surrounding passive areas (cathode) during sliding, thus causes a significant negative shift in OCP. And after that, the OCP reaches a new

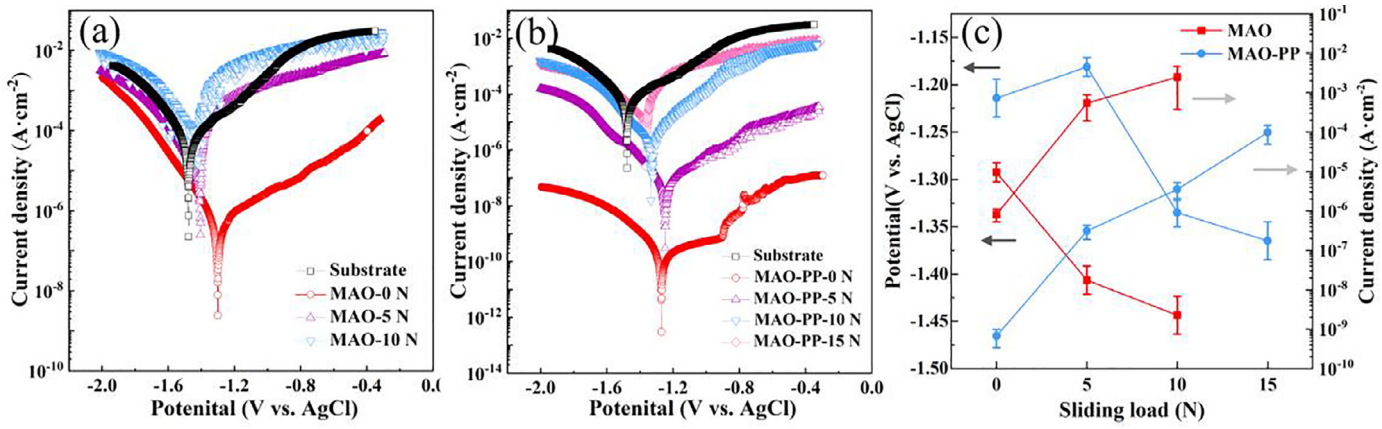

Fig. 14. Potentiodynamic polarization curves under different loads after sliding 1800 s of MAO (a) and MAO-PP sample (b), and the evolution of E_{corr} and i_{corr} as a function of sliding load (c).

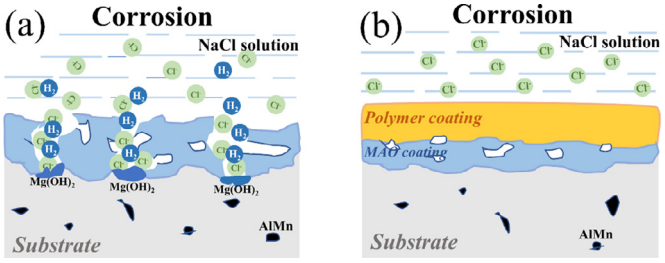

Fig. 15. Schematic of the proposed corrosion mechanisms for MAO sample (a) and MAO-PP sample (b).

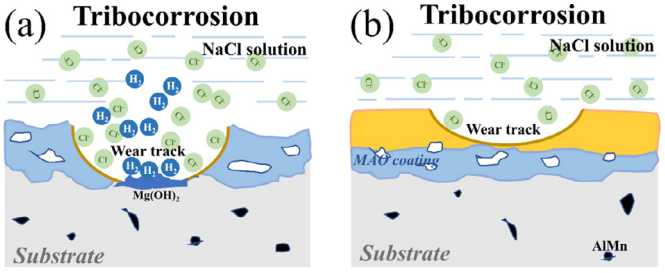

Fig. 16. Schematic draws of the suggested tribocorrosion under 10 N load mechanisms for MAO sample (a) and MAO-PP sample (b).

steady state due to the establishment of an equilibrium between the depassivation and repassivation rates in the wear track [35]. The sliding process could accelerate the corrosion rate of the exposed Mg alloy substrate with corrosive medium in the 3.5 wt.% NaCl solution, resulting in the larger i_{corr} value of MAO sample under 10 N load sliding than that of Mg substrate. Also, the MAO coating has poor wear resistance and has been worn out under 10 N load, as shown in Fig. 16 (a). However, the MAO-PP sample shows much smaller wear track than the MAO sample due to its lower friction coefficient and higher wear resistance. And the MAO coating as the interlayer is hardly destroyed during tribocorrosion under 10 N load and could protect the substrate from the corrosive medium, as illustrated in Fig. 16 (b). Thus, the i_{corr} value of the MAO-PP sample during tribocorrosion under 10 N load is lower than that of the Mg alloy substrate, indicating that the composite coating could still prevent the intrusion of Cl^- ions and provide protection to the substrate under sliding process.

4. Conclusions

A composite coating combined a MAO coating and a polymer coating for improving tribocorrosion resistance of Mg alloy is fabricated. The polymer coating is comprised of polyamide-imide (PAI) and polytetrafluoroethylene (PTFE). The composite coating could effectively prevent the corrosive medium from penetrating into the interface between the MAO coating and Mg alloy substrate, resulting an excellent anti-corrosion performance. Meanwhile, the composite coating endows other properties, including hydrophobic, low friction coefficient, and high wear resistance. Furthermore, the composite coating possesses much better tribocorrosion resistance than the single MAO coating. This work is expected that inspires the development of MAO-based duplex coating, which would provide other properties besides excellent anti-corrosion performance and further extend the application fields of Mg alloy.

Declaration of Competing Interest

The authors declare that they have no known competing financial interests or personal relationships that could have appeared to influence the work reported in this paper.

CRediT authorship contribution statement

Siqin Liu: Conceptualization, Methodology, Investigation, Visualization, Writing – original draft, Writing – review & editing. **Guihua Li:** Methodology, Investigation. **Yuming Qi:** Investigation, Visualization. **Zhenjun Peng:** Data curation, Investigation. **Yinping Ye:** Methodology, Supervision, Validation. **Jun Liang:** Methodology, Project administration, Supervision, Validation, Writing – review & editing.

Acknowledgments

The authors are grateful to the financial supports of National Natural Science Foundation of China (Grant No.52071325).

References

[1] H. Mraied, W. Wang, W. Cai, J. Mater. Chem. B 7 (2019) 6399–6411.
[2] M. Esmaily, J.E. Svensson, S. Fajardo, N. Birbilis, G.S. Frankel, S. Virtanen, R. Arrabal, S. Thomas, L.G. Johansson, Prog. Mater Sci. 89 (2017) 92–193.
[3] S.V. Lamaka, B. Vaghefinazari, D. Mei, R.P. Petrauskas, D. Hoche, M.L. Zheludkevich, Corros. Sci. 128 (2017) 224–240.
[4] S. Siddique, A.A. Bernussi, S.W. Husain, M. Yasir, Surf. Coat. Technol. 394 (2020).
[5] Q. Li, H. Lu, D.Y. Li, Wear 426-427 (2019) 981–988.
[6] J. Sudagar, J.S. Lian, X.M. Chen, P. Lang, Y.Q. Liang, T. Nonferr. Met. Soc. 21 (2011) 921–928.
[7] H. Li, X. Feng, Y. Peng, R. Zeng, Nanoscale 12 (2020) 7700–7711.
[8] B. Zhang, R. Yao, L. Li, Y. Wang, R. Luo, L. Yang, Y. Wang, ACS Appl. Mater. Interfaces 11 (2019) 41165–41177.
[9] H. Wei, Y. Wang, J. Guo, N.Z. Shen, D. Jiang, X. Zhang, X. Yan, J. Zhu, Q. Wang, L. Shao, H. Lin, S. Wei, Z. Guo, J. Mater. Chem. A 3 (2015) 469–480.
[10] C.D. Gu, W. Yan, J.L. Zhang, J.P. Tu, Corros. Sci. 106 (2016) 108–116.
[11] C. Liu, T. Xu, Q. Shao, S. Huang, B. Jiang, J. Liang, H. Li, J. Alloys Compd. 784 (2019) 414–421.
[12] T. Dao, P.D. Ducharme, U.M. Tefashe, J.R. Kish, J. Mauzeroll, Anal. Chem. 84 (2012) 9899–9906.
[13] T.W. Clyne, S.C. Troughton, Int. Mater. Rev. 64 (2019) 127–162.
[14] X.X. Dan Jiang, Jian Hou, Guangyi Cai, Xinxin Zhang, Zehua Dong, Chem. Eng. J. 373 (2019) 285–297.
[15] D.K. Ivanou, M. Starykevich, A.D. Lisenkov, M.L. Zheludkevich, H.B. Xue, S.V. Lamaka, M.G.S. Ferreira, Corros. Sci. 73 (2013) 300–308.
[16] M. Toorani, M. Aliofkhazraei, Surf. Interfaces 14 (2019) 262–295.
[17] W. Yu, R. Sun, Z. Guo, Z. Wang, Y. He, G. Lu, P. Chen, K. Chen, Appl. Surf. Sci. 464 (2019) 708–715.
[18] D. Jiang, H. Zhou, S. Wan, G.Y. Cai, Z.H. Dong, Surf. Coat. Technol. 339 (2018) 155–166.
[19] D.K. Ivanou, K.A. Yasakau, S. Kallip, A.D. Lisenkov, M. Starykevich, S.V. Lamaka, M.G.S. Ferreira, M.L. Zheludkevich, RSC Adv. 6 (2016) 12553–12560.
[20] Z. Zheng, M.C. Zhao, L. Tan, Y.C. Zhao, B. Xie, D. Yin, K. Yang, A. Atrens, Surf. Coat. Technol. 386 (2020).
[21] C.M. Ning, X.J. Cui, L.L. Shang, Y.J. Zhang, G.A. Zhang, Diamond Relat. Mater. 106 (2020).
[22] D. Jiang, X. Xia, J. Hou, X. Zhang, Z. Dong, Ind. Eng. Chem. Res. 58 (2019) 165–178.
[23] S.Y. Kim, Y.K. Kim, M.H. Ryu, T.S. Bae, M.H. Lee, Sci. Rep. 7 (2017) 9061.
[24] F.C. Walsh, C.T.J. Low, R.J.K. Wood, K.T. Stevens, J. Archer, A.R. Poeton, A. Ryder, T. I. Met. Finish. 87 (2009) 122–135.
[25] X.J. Cui, X.Z. Lin, C.H. Liu, R.S. Yang, X.W. Zheng, M. Gong, Corros. Sci. 90 (2015) 402–412.
[26] P. Vengatesh, M.A. Kulandainathan, ACS Appl. Mater. Interfaces 7 (2015) 1516–1526.
[27] D. Mashtalyar, K. Nadaraia, S. Sinebryukhov, S. Gnedenkov, Mater. Today Proc. 11 (2019) 150–154.
[28] Y. Ma, H. Wan, Y. Ye, L. Chen, H. Li, H. Zhou, J. Chen, Tribol Int 148 (2020).
[29] Z. Lv, S. Yu, K. Song, X. Zhou, X. Yin, Prog. Org. Coat. 147 (2020) 105723.
[30] H. Lao, N. Mushtaq, G. Chen, H. Jiang, Y. Jiao, A. Zhang, X. Fang, Polymer (2020) 122889.
[31] G. Zhang, L. Wu, A. Tang, X. Ding, B. Jiang, A. Atrens, F. Pan, Prog. Org. Coat. 132 (2019) 144–147.
[32] Z. Ur Rehman, D. Choi, J. Magnes. Alloy. 7 (2019) 555–565.
[33] G. Zhang, L. Wu, A. Tang, B. Weng, A. Atrens, S. Ma, L. Liu, F. Pan, RSC Adv. 8 (2018) 2248–2259.
[34] Z. Li, W. Yang, Q. Yu, Y. Wu, D. Wang, J. Liang, F. Zhou, Langmuir 35 (2019) 1134–1145.
[35] B. Zhang, J. Wang, F. Yan, Corros. Sci. 131 (2018) 252–263.
[36] C. Martini, L. Ceschini, F. Tarterini, J.M. Paillard, J.A. Curran, Wear 269 (2010) 747–756.
[37] Y. Ma, Y. Ye, H. Wan, L. Chen, H. Zhou, J. Chen, Tribol. Lett. 67 (2019).
[38] C. Yu, P. Ju, H. Wan, L. Chen, H. Li, H. Zhou, J. Chen, Prog. Org. Coat. 145 (2020) 105667.
[39] Z. Yao, Z. Jiang, X. Sun, S. Xin, Z. Wu, Mater. Chem. Phys. 92 (2005) 408.
[40] J Liang, L Hu, J Hao, Appl. Surf. Sci. 253 (2007) 6939–6945.
[41] J. Liang, P.B. Srinivasan, C. Blawert, W. Dietzel, Electrochim. Acta 55 (2010) 6802–6811.
[42] V.G. Pina, V. Amigó, A.I. Muñoz, Corros. Sci. 109 (2016) 115–125.